Membrane Interactions, Ligand-Dependent Dynamics, and Stability of Cytochrome P4503A4 in Lipid Nanodiscs

Nicholas A. Treuheit, **Michelle Redhair**, **Hyewon Kwon**, **Wynton D. McClary**, **Miklos Guttman**, **John P. Sumida**, and **William M. Atkins**[*]

Department of Medicinal Chemistry, University of Washington, Box 357610, Seattle, Washington 98195-7610, United States

Abstract

Membrane-bound cytochrome P4503A4 (CYP3A4) is the major source of enzymatic drug metabolism. Although several structural models of CYP3A4 in various ligand complexes are available, none includes a lipid bilayer. Details of the effects of the membrane on protein dynamics and solvation, and access channels for ligands, remain uncertain. H/D exchange mass spectrometry (H/DXMS) with ligand free CYP3A4 containing a deletion of residues 3–12, compared to that of the full length wild type, in lipid nanodiscs afforded 91% sequence coverage. Deuterium exchange was fast in the F- and G-helices, HI loop, and C-terminal loop. In contrast, there is very low exchange in the F′-and *G′*-helices. The results are consistent with the overall membrane orientation of CYP3A4 suggested by published MD simulations and spectroscopic results, and the solvent accessibility of the F/G loop suggests that it is not deeply membrane-embedded. Addition of ketoconazole results in only modest, but global, changes in solvent accessibility. Interestingly, with ketoconazole bound some peptides become less solvent accessible or dynamic, including the F- and G-helices, but several peptides demonstrate modestly increased accessibility. Differential scanning calorimetry (DSC) of CYP3A4-nanodiscs suggests membrane-induced stabilization compared to that of aggregated CYP3A4 in buffer, and this stabilization is enhanced upon addition of the ligand ketoconazole. This ligand-induced stabilization is accompanied by a very large increase in ΔH for CYP3A4 denaturation in nanodiscs, possibly due to increased CYP3A4–membrane interactions. Together, the results suggest a distinct orientation of CYP3A4 on the lipid membrane, and they highlight likely solvent access channels, which are consistent with several MD simulations.

Graphical Abstract

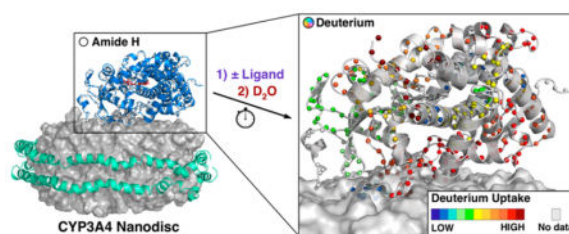[*]Corresponding Author: Tel: 206 685-0379. winky@uw.edu.

Hepatic cytochrome P450s (CYPs) play a critical role in chemical detoxication and drug metabolism by oxidizing a wide range of structurally unrelated xenobiotics.[1,2] Among human membrane-bound CYPs, CYP3A4 dominates drug metabolism.[3,4] CYP3A4 has been extensively characterized by an impressive array of spectroscopic methods, kinetic methods, and structural techniques.[5–9] In particular, crystallographic analyses have provided detailed models of the ligand–protein interactions and ligand-dependent conformational changes that are coupled to catalytic turnover or inhibition by various compounds.[8,9] However, the majority of these analyses have been done in the absence of a lipid membrane. As a result, the effects of membrane–protein interactions on CYP3A4 structure, function, and dynamics remain incompletely characterized.[10]

Recent studies have focused on the details of the orientation of CYP3A4 and other isoforms, in the membrane bilayer, and on solvent access channels that may control substrate access to and product egress from the active site.[10–14] Typical drug substrates for CYP3A4 are extremely hydrophobic and are expected to enter the active site via the membrane.[8,9,15] However, small polar diatomic molecules are also known to access the active site and ligate to the heme iron.[16] In fact, the interaction of water with the heme is a critical aspect of the catalytic cycle, but its access to the heme has not been mapped experimentally.[16] The wide range of physical properties among ligands that access the heme of CYP3A4 suggests the possibility of multiple distinct channels.

Molecular dynamics simulations have provided hypothetical models for the orientation of CYP3A4 in the membrane and possible routes of entry for hydrophobic substrates and water.[10,12–14,17] However, very few experimental data are available to challenge these models. Here, we provide the first analysis of ligand-dependent changes in solvent accessibility and thermal stability of any CYP in a lipid bilayer. Specifically, we performed H/DXMS and differential scanning calorimetry on CYP3A4 in lipid nanodiscs. The results confirm several structural and dynamic features of recently proposed models, and they reveal a map of the dynamic features of CYP3A4 in a lipid bilayer. Specifically, the H/DXMS data indicate that the solvent accessibility of CYP3A4 is nearly identical in detergent solution compared to that in nanodiscs. Whereas the F′- and G′-regions exhibit low H/D exchange, the F- and G-helices are highly solvent accessible, or their interaction with the membrane phospholipid head groups facilitates exchange and water recruitment. Also, there is a significant thermal stabilization of CYP3A4 incorporated in nanodiscs compared to that of CYP3A4 in solution, as well as for ketoconazole-bound CYP3A4 in nanodiscs. In fact, there is a very large ligand-induced increase in ΔH for unfolding of CYP3A4 in the nanodiscs, which could be due to modestly increased interactions with the membrane.

MATERIALS AND METHODS

Expression and Purification of CYP3A4

Recombinant CYP3A4 was expressed as described previously.[18,19] Briefly, CYP3A4 was expressed in *E. coli* C41(DE3) cells transformed with pCWOri+ encoding ampicillin resistance and a CYP3A4 gene with an N-terminal deletion of residues 3–12 and further modified with a C-terminal His tag. The truncation eliminates amino acids 3–12 from the wild type CYP3A4 sequence, and the protein includes a serine-to phenylalanine substitution at position 18. A combination of lysozyme and French press were used to lyse the cells. Protein was then purified first with a Ni-NTA affinity column followed by a hydroxyapatite ion exchange column. Purified protein was then dialyzed into storage buffer [100 mM KP_i, 20% glycerol, 1 mM EDTA, and 500 μM TCEP (pH 7.4)] and stored in 1 mL aliquots at ~25 μM at −80 °C for further use. Aliquots were typically not used after a single freeze–thaw. Protein concentration was determined using a similar method to that of Omura and Sato[20] with an extinction coefficient of 104 mM^{-1} cm^{-1} for the ferric enzyme.

Expression and Purification of MSP1D1

Expression and purification of the nanodisc scaffold protein MSP1D1 were performed as described previously.[21,22] Briefly, MSP1D1 was expressed in *E. coli* BL21-Gold (DE3) cells transformed using a pET expression vector encoding kanamycin resistance with a C-terminal His tag connected by a TEV protease cleavage site. Cells were lysed using a French press, and after separation by ultracentrifugation (100000g for 1 h at 4 °C), the lysate supernatant was purified with a Ni-NTA affinity column followed by dialysis into standard buffer (50 mM Tris, 100 mM NaCl, and 0.5 mM EDTA at pH 7.4). Pro-TEV Plus (Promega Corporation) was used to remove the His tag according to the established protocol, and then, MSP1D1 without its His tag, MSP1D1(−), was purified again with a Ni-NTA column, dialyzed into standard buffer, and stored in 1 mL aliquots at −20 °C. Protein concentration was determined by absorbance at 280 nm using calculated extinction coefficients ($\varepsilon_{280\ nm}$ (MSP1D1(+)) = 21430 M^{-1} cm^{-1}; ε_{280} (MSP1D1(−)) = 18450 M^{-1} cm^{-1}).

Self-Assembly of Nanodiscs

CYP3A4-nanodiscs were prepared in a similar manner as described previously.[21,23] A POPC film was dried in a vacuum desiccator overnight in preparation. CYP3A4, MSP1D1(−), and POPC were mixed in a 0.1:1:65 molar ratio with 50 mM sodium cholate and incubated on a shaker at 4 °C for 1 h. Washed Amberlite XAD-2 beads (hydrophobic adsorbent resin) were added at 0.5 g/mL to the protein mixture in order to remove the detergent and initiate self-assembly. The mixture was returned to the shaker at 4 °C for 4 additional hours. Ni-NTA column chromatography was used to purify the 3A4 nanodiscs from both empty nanodiscs and excess POPC. The 10-fold excess of MSP1D1 helped ensure that only one monomer of CYP3A4 was incorporated into a single nanodisc. Size exclusion chromatography (SEC) on a Superdex 200 10/300 GL column (GE Healthcare) was used to verify stable incorporation of 3A4 into nanodiscs, measuring absorbance at 420 and 280 nm (Supporting Information, Figure S1). SEC demonstrates resolution of CYP3A4 (21 min retention time) from empty nanodiscs (25 min retention time) and CYP3A4 nanodiscs (23 min retention time). Also, SEC with a mixture of empty nanodiscs and free CYP3A4 yields

a chromatogram with a heme-protein peak at 21 min and a protein peak at 25 min, and no peak at 21 min (Supporting Information, Figure S2). A difference spectrum of [ferrous CO-bound CYP3A4–ferrous CYP3A4] was used to calculate the P420 content in the nanodiscs of 7%.

Differential Scanning Calorimetry

DSC experiments were performed using a MicroCal VP-Capillary DSC System (MicroCal, Northampton, MA). Nanodisc samples were diluted to 5 μM in a final volume of 500 μL and dialyzed overnight against disc forming buffer (100 mM potassium phosphate and 50 mM sodium chloride at pH 7.4). The instrument was primed by performing three consecutive scans of disc forming buffer before analysis of a single sample. DSC thermograms were generated by scanning from 10 to 130 °C at a scan rate of 60 °C/h. Transition temperatures and enthalpies of the transitions were determined by fitting the data using the software package Origin (MicroCal).

Hydrogen/Deuterium Exchange Mass Spectrometry

Deuterium exchange of CYP3A4 nanodiscs was carried out as described previously for other proteins by Parker et al.[24,25] Standard hydrogen–deuterium exchange practices were applied with a few additional steps to account for disassembly of the nanodiscs and removal of the excess POPC from solution prior to MS analysis. Ten micromolar 3A4-nanodisc samples, with or without 100 μM ketoconazole, were diluted 10-fold into 50 mM Tris, 100 mM NaCl, pD 7.4, and 99% deuterium oxide. After 0 s, 10 s, 30 s, 1 min, 2 min, 10 min, and 24 h at 25 °C, the entire sample was quenched 1:1 with cold quench buffer (300 mM KPi, 4 M guanidine-HCl and 0.25 M Tris-carboxyethane-phosphate [TCEP] at pH 2.5), and nanodisc disassembly was facilitated by the addition of a 25-fold excess of sodium cholate in relation to nanodisc concentration. Then, the entire mixture was immediately added to cold immobilized pepsin (Pierce). Samples were stored on ice with frequent mixing for 4 min, after which 10 mg of ZrO_2-coated silica resin (Hybrid SPE resin, Sigma) was added to the digestion mixture to remove excess POPC and stored again on ice for an additional 60 s. The entire sample was passed across a chilled filter (0.45 μm cellulose acetate) to remove pepsin beads, ZrO_2 resin, and precipitated cholate before being immediately separated into aliquots and flash frozen in liquid nitrogen for storage at −80 °C.

Chromatography was performed on a Waters nanoACQ-UITY UPLC system, where samples were thawed on ice for 5 min and injected on a Vanguard BEH Shield RP18 1.7 μm trap column (2.1 × 5 mm; Waters) flowing 0.1% formic acid (FA) with 0.02% trifluoroacetic acid (TFA) at 100 μL/min to load the peptides. After a 3 min wash, peptides were diverted onto a Hypersil 1.9 μm C_{18} column (1 × 50 mm; Thermo Scientific) using a gradient of 15 to 40% solvent B for 8 min (solvent A, 0.1% FA, 0.02% TFA, and 5% acetonitrile [ACN]; solvent B, 0.1% FA and 0.02% TFA 80% ACN). At the end of the UPLC gradient, sample flow from the column was diverted away from the MS source to prevent unnecessary flow of excess cholate into the mass spectrometer. The syringe, loop, and trap column were cleaned between sample injections with sample loop volume injections of 10% formic acid, 80% methanol, 2:1 isopropanol-ACN, and 80% ACN. To avoid carryover, the column was cleaned with two rapid (10 to 100% solvent B for 30s) gradients at the end of each sample

run. A Waters Synapt G2-S Q-TOF mass spectrometer was used to analyze eluting peptides with desolvation temperatures of 80 and 150 °C. The column, injection loop, and lines were kept at 0.5 °C in a separate cooler unit to minimize back exchange. CYP3A4 peptide identities were acquired using PLGS Version 3 (Waters), by analyzing ion-mobility MS^E data against a library comprising the sequences of CYP3A4, MSP 1D1, and porcine pepsin, which helped to further distinguish peptides unique to CYP3A4 from the scaffold protein and digestion mixture. Specifically, peptides were identified using criteria of a maximum of 3 ppm error in parent mass assignments, a minimum of 5 y- or b-ions in MS^E data, and a minimum PLGS score of 7.5. Deuterium shifts were calculated using DynamX Version 3 (Waters) Deuterium levels were not corrected for back-exchange and are therefore reported as relative as justified by others.[26]

Ketoconazole was dissolved to 9 mg/mL (17 mM) in ethanol. It was added to 10 μM nanodisc samples for a final concentration of 100 μM, with the expected generation of type II difference spectrum (not shown) and incubated for 5 min on ice before beginning deuterium exchange according to the same methods as that used for the ligand-free samples.

RESULTS

Differential Scanning Calorimetry

As an initial probe of monomeric CYP3A4 dynamics and solvent exposure in a membrane bilayer, DSC was used to determine the melting temperature (T_m), in the absence and presence of the CYP3A4 substrate ketoconazole. DSC provides a relative measure of the thermal stability of a folded protein, which typically changes upon its interaction with a stabilizing partner such as a ligand, another protein, or a membrane.[26,27] As solvent channels are restricted and proteins become more compact, the T_m typically shifts to higher temperatures. However, in contrast to a vast literature concerning DSC with soluble proteins, DSC with membrane proteins is largely unexplored and previously unreported for protein in nanodiscs. Speculatively, two limiting cases can be considered concerning the thermal transitions expected for a protein–nanodisc particle. Specifically, in one case it would be expected that a protein deeply embedded in the membrane of a nanodisc would lead to a cooperative thermal denaturation of the entire "particle" including the embedded protein, the scaffold protein, and lipid bilayer. This would be expected to happen at a temperature at least as high as the higher T_m of either the individual embedded protein or the individual nanodisc. In contrast, if the protein was embedded in the membrane via only a single anchor helix as expected for CYP3A4 and the remainder was only superficially interacting with the lipids, then its thermal denaturation and the denaturation of the nanodisc would possibly occur separately or sequentially, with minimal effect of each component of the other. Multiple thermal transitions would be observed corresponding to the target protein or to the nanodisc. If the monotopic membrane protein such as CYP3A4 interacted with the membrane interface, then its thermal denaturation would likely be affected, but the effects would not be predictable based on experience with soluble proteins. Because the thermal denaturation of peripheral membrane proteins on a membrane surface is not well-characterized, there are no clear experimental benchmarks for this situation. However, it is reasonable to speculate that the DSC of the protein would be more complex than two state

unfolding of soluble proteins, wherein protein–membrane interactions would also contribute. We hypothesized that these limiting cases provide qualitative benchmarks for the behavior of intrinsic membrane proteins vs monotopic peripheral membrane proteins and that CYP3A4 in nanodiscs would behave more like the latter. For the sake of comparison, DSC was also performed with CYP3A4 in buffer, which is an aggregate of CYP3A4, based on size exclusion chromatography (Supporting Information). DSC results are shown in Figure 1.

Conveniently, the phase transition of POPC bilayers of the nanodiscs used here is sufficiently low (4 °C) to not interfere with the typical thermal transitions of proteins (40 °C–65 °C). Furthermore, the empty nanodiscs exhibit no thermal transitions below 60 °C. At ~70 °C–100 °C, the empty nanodiscs denature and yield the observed exothermic transition. So, the nanodiscs contribute no DSC response in the temperature range 35 °C–65 °C, where the CYP3A4 nanodiscs clearly yield a set of overlapping transitions. In addition, the thermogram for aggregated CYP3A4 in buffer, not incorporated in nanodiscs, is shown in Figure 1. It is clear that incorporation into nanodiscs has a significant stabilizing effect on CYP3A4 compared to its aggregated state in buffer, and the addition of ketoconazole further stabilizes the CYP3A4. The model-independent calorimetric ΔH's measured directly for each entire thermogram are reported in Table 1 along with the T_m for the highest transitions. A more detailed analysis of the thermodynamic parameters associated with the complex transitions is reported in Supporting Information and Table S1, and includes a comparison of calorimetric enthalpy and van't Hoff enthalpy for each of the deconvoluted transitions that comprise the overall thermograms (Figure S3). The discrepancy between calorimetric enthalpy and van't Hoff enthalpy for most of the deconvoluted transitions clearly indicates they are not two-state processes. Because there are no experimental benchmarks for interpreting this behavior with membrane-associated proteins, we focus here only on the model-independent parameters in Table 1.

A striking result is the very significant increase in T_m (~ 7 °C) for thermal denaturation of CYP3A4 in the nanodisc upon addition of a saturating concentration of ketoconazole, compared to in the absence of ligand. Furthermore, the complexity of the thermogram increases and the overall calorimetric ΔH nearly doubles in the presence of ketoconazole. These very large ligand-induced changes are much greater than the modest increase in ΔH and T_m in the absence of the nanodisc (Table 1). This is possibly due to a change in ligand-induced CYP3A4–membrane interactions, as discussed further below regarding H/DX behavior.

Also, the thermal transitions corresponding to the nanodiscs are shifted from ~77 °C in the absence of CYP3A4 to ~85 °C–90 °C when CYP3A4 is included, suggesting that the CYP3A4 stabilizes the nanodisc slightly, as would be expected for a peripheral membrane protein with a single helix inserted in the membrane. This is accompanied by a very large increase in calorimetric enthalpy for the nanodiscs denaturation (Table 1). Just as the scaffold proteins of the nanodisc interact with lipids to form an ordered lipid boundary layer,[28,29] the inserted N-terminus of the CYP3A4 could result in more ordered lipids with a resulting increase in ΔH for their temperature-induced denaturation.

Together, the results demonstrate a clear membrane-induced stabilization of CYP3A4 and ketoconazole-induced stabilization of CYP3A4 that is not entirely deeply embedded in the membrane. This suggests that upon addition of ketoconazole, the CYP3A4 protein is more tightly packed or more intimately interacting with the membrane, and presumably this corresponds to a decrease in solvent accessibility in some regions of the protein.

CYP3A4 Solvent Accessibility in Nanodiscs by H/ DXMS

To determine the relative solvent accessibility of specific peptides contained in the membrane-bound CYP3A4, amide H/DXMS experiments were performed in which CYP3A4 nanodiscs were exposed to D_2O for variable periods of time ranging from 0 s to 24 h. After exposure to D_2O, CYP3A4 nanodisc disassembly and digestion were performed as described above, modified from previously published experiments (Figure 2B; refs 24, 25, and 30). Figure 2A includes a schematic of CYP3A4 with a possible orientation with respect to a membrane, based on available models. Digestion conditions were optimized by the addition of 2 M guanidine HCl in the final quench mixture. This greatly increased the peptide signal and subsequent fragment identification. Using LC-ESI-MS^E, more than 60 unique peptides were identified in CYP3A4 that also included quality deuterium uptake profile. This accounts for a linear sequence coverage of 91% (Figure 3A), which is significantly greater than obtained in H/DXMS studies with other proteins in nano-discs.[24,25] Additionally, overlapping peptides were identified in multiple regions, providing further support for our deuterium uptake profiles.

The deuterium uptake profiles for the peptides comprising CYP3A4 in the primary sequence are summarized in Figure 3A, and their corresponding locations in the folded structure are shown in Figure 3B. The relative extent of H/D exchange at seven time points of the identified peptides are mapped onto the linear peptide sequence, which demonstrates clearly resolved regions of varying exchange. The location of these peptides in the tertiary structure is shown in Figure 3B. Our data represent the time-dependent exchange of nearly the entire folded structure of CYP3A4 in the nanodisc membrane.

H/DXMS of CYP3A4 in Detergent Solution

In order to compare the solvent accessibility and dynamics of CYP3A4 in nanodiscs with detergent-solubilized CYP3A4, we also performed HDXMS in 0.1% Emulgen buffer. This is a commonly used detergent for *in vitro* CYP3A4 experiments. Direct comparisons of structure and dynamics of CYPs in nanodiscs and detergent solution are lacking, and modest differences in functional behavior in the two environments have not been explained. Interestingly, attempts to measure H/DX for CYP3A4 in buffer without Emulgen, and not in nanodiscs, yielded poor signal and poor sequence coverage (not shown). Also, although it might be expected that Emulgen would monomerize CYP3A4, our SEC analysis of CYP3A4 in 0.1% Emulgen did not indicate a homogeneous monomer. It is a complex mixture with aggregates (not shown). Therefore, we caution against comparing DSC data in buffer with HD/XMS data in Emulgen due to possible differences in aggregate structure. It is still useful to compare H/DX in Emulgen with CYP3A4 in nanodiscs to determine whether protein fold or conformation is affected. Results for the Emulgen solution are summarized in Figure 4, which includes a "butterfly plot" of the H/DX in nanodiscs vs the

H/DX in Emulgen (Figure 4A). The high degree of symmetry with respect to the "zero exchange" demonstrates that the solvent accessibility is very similar in nanodisc and Emulgen. A plot of the difference (Figure 4B) reveals modest differences mainly localized in the F- and G-helices; the H/D exchange is ~20% greater at the early time points (10 s and 30 s) for the Emulgen samples compared to the nanodisc samples, and these differences become smaller at longer time points, as expected. These data suggest that the membrane interactions with the F- and G-helices are not perfectly mimicked by the detergent. Together, the data indicate that the lipid bilayer provides some protection from solvent for the F- and G-helices compared to that of the protein in detergent solution, even though they remain highly exchangeable when CYP3A4 is in the membrane. Also, it is highly significant that there is increased peptide coverage at the N-terminus in the Emulgen samples compared to that in the nanodisc samples. Two additional peptides spanning residues 33–51 of CYP3A4 were identified in the Emulgen samples that could not be recovered in the nanodiscs samples. Residues 33–51 include the last half of the A″-helix, the A-anchor, and the first half of the A′-helix. This is further confirmation that these residues interact very intimately with the membrane bilayer and become accessible in its absence.

Effects of Ketoconazole on H/D Exchange

The crystal structure of the ketoconazole complex of CYP3A4, which lacks the N-terminal transmembrane helix, suggests relatively subtle but wide ranging conformational changes upon binding.[9] In order to assess possible effects of the membrane on ligand-induced conformational change, we performed H/DXMS with the [CYP3A4·ketoconazole] complex in nanodiscs. The H/ DXMS results are remarkably consistent with the change in solvent accessibility suggested by the crystal structure. Figure 5 summarizes the effects of ketoconazole. Figure 5A and B are butterfly plots of ligand free vs ketoconazole bound and their difference, respectively. The four regions that exhibit significant protection in the presence of ketoconazole (% exchange >5%) are colored dark blue in the tertiary structure (Figure 5C) and highlighted in the difference plot (Figure 5B). The protected regions include (1) the A helix, (2) the G-helix and the loop preceding the H-helix, (3) the middle of the I-helix, and (4) the loop between the K-helix and the β1 sheet. Additional regions with modest protection in the presence of ketoconazole (2% > % exchange >5%) are colored light blue in the tertiary structure (Figure 5C) and highlighted in the difference plot (Figure 5B). Interestingly, two regions become more solvent exposed in the presence of ketoconazole (−2% > % exchange > −5%) and are colored red in the tertiary structure (Figure 5C) and highlighted in the difference plot (Figure 5B). The regions that are less protected include (1) the C-helix and (2) the J-helix and the loop preceding the J′-helix. It should be emphasized that the precision of H/DX is within these measured differences, which are observed in multiple overlapping peptides, and differences of >2% were observed for these peptides in at least two separate experiments. This change in mass is easily resolvable for peptides with the molecular weights obtained in our experiments.

DISCUSSION

The studies included here represent the first H/DXMS analysis of any CYP in a lipid bilayer, and the DSC experiments are the first of any membrane protein in a lipid nanodisc, of which

we are aware, although empty nanodiscs with other lipids have been studied by DSC and other mass spectrometry methods.[31–33] Together, the studies provide new information about (1) the membrane topology and orientation and some of the resulting access channels for solvent or possibly substrates to the active site; (2) the effect of a substrate on solvent accessibility of CYP3A4 in a membrane; (3) the effect of ketoconazole on the thermal stability of membrane bound CYP3A4; and (4) the overall solvent accessibility of CYP3A4, which is nearly identical in detergent solution and in membrane nanodisc, but the dynamics of the F- and G-helices or their solvent accessibility are not identical.

The solvent accessibility profile for ligand-free CYP3A4 in nanodiscs, shown in Figure 3, presents a number of interesting observations. As expected, the I-helix that is buried in the interior of the protein exhibits low solvent accessibility. A number of other peptides along the "backside" of CYP3A4 and expected to face away from the membrane, including the D-, E-, F-, and G-helices, show relatively high solvent accessibility. Previously published simulations by others[17,34] suggest dramatic rearrangement and varying degrees of insertion of CYP3A4 upon interaction with a membrane.

In particular, Baylon et al.[17] and Denisov et al.[10] show based on MD simulation that the elements that interact most with the membrane are the deeply embedded N-terminal helix and A-anchor, between A″- and A′-helices, and the F′/G′-helices. This membrane penetration of the F′- and G′-helices is in strong agreement with our experimental H/DXMS data, which exhibit slow exchange along this interface. In fact, it is striking that the N-terminus that is near the F′/G′ region in the folded structures is among the very few regions not recovered in our workup. Our coverage includes only the C-terminal few residues of the A′-helix that precede the A-helix. The lack of coverage in this localized regions compared to the near complete coverage throughout the rest of the sequence suggests, indirectly, that the N-terminus is intimately embedded in the membrane and therefore difficult to recover in the postincubation workup. This is consistent with essentially all of the previously published simulations.

Additionally, the C-, D-, and E-helices have been predicted on the basis of MD simulations to not be in direct contact with the membrane,[10,17,34] which is reflected in higher solvent accessibility profiles in our experiments. However, in our experiments, we observe a remarkably high degree of solvent deuterium exposure in the F- and G-helices and the B/C loop, which is consistent with the simulation work by Baylon et al.,[17] particularly along the relatively exposed B/C loop. In addition, the simulations of Berka et al.[34] suggest that the F′/G′-helices-loop and a large portion of the F- and G-helices are deeply embedded in the membrane and should exhibit less H/D exchange. They note, however, that portions of the F- and G-helices are in contact with polar lipid head groups. Our results are inconsistent with the entire F/G-helices being deeply embedded in the membrane. However, to the extent that the polar lipid head groups may not completely shield the protein from solvent, our results strongly suggest the likelihood that that portions of the F- and G-helices are on the lipid surface and not deeply embedded in the membrane, consistent with the suggestion by Berka et al. Interestingly, the simulations performed by Baylon et al. included truncated, short, acyl chains of the lipids, which would be expected to result in decreased hydrophobic effects and possibly underestimate the strength of the interactions between the native membrane and the

F/G-helices. However, their models are remarkably aligned with our results. Unexpectedly, the region of CYP3A4 near the F- and G-helices is the *most* solvent accessible of any regions in CYP3A4, in contrast to some surface loops that face the cytosol. Multiple sequential and overlapping peptides confirm this result. In fact, it is important to emphasize that the set of overlapping peptides includes small peptides (6–8 residues) on the C-terminal end and the N-terminal end of the F- and G-helices. These F- and G-helix peptides are the ends of these helices closest to the F′G′-region and thus might expected to be protected by the membrane, yet they are highly solvent exposed.

The combination of the results demonstrating that the N-terminus and F′/G′-helices form the only embedded membrane anchor points, together with the expectation that the F- and G-helices and F/G loop provide a hydrophobic conduit for substrates entering from the membrane, suggests the possibility that the F/G-helices of CYP3A4 are capable of transiently "bouncing" on and off the membrane or translating across it. This would create transient hydrophobic channels in the F/G loop region that are in contact with the membrane, while other portions anchor the entire molecule to the bilayer. In fact, we propose that some portions of the F/G-helix region transiently sample the surface and upper hydrophobic region of the lipid hydrocarbon chains, based on their unexpectedly high solvent accessibility despite their highly hydrophobic character. The F- and G-helical regions could be transiently moving between the hydrophobic region and the surface of the membrane, while the F′/G′-helices and loop, along with the N-terminal region, provide a membrane-anchored "hinge".

Any subtle variance between the simulations of different groups and some of our experimental data could be a result of (1) the slight N-terminal truncation that is used in our CYP3A4 construct and the simulations by Denisov et al.,[10] but not Berka et al.,[17] yielding a much shallower insertion into the nanodisc for the former; (2) the nanodisc lipid packing could be different from other membrane environments and disfavor deep insertion of the protein; and (3) some of the MD simulations could overemphasize the lipid protein interactions and yield an artificially "deep" insertion. Interestingly, there is precedent for protein–lipid interfaces promoting water access to a higher degree than bulk lipid phases.[35] Alternatively, increases in local charge can accelerate H/DX in proteins.[36] Regardless of the source of the differences, the H/DX MS data clearly confirm the role of the A-helix, $\beta 1,2$, and nearby F′/G′-regions as the strongest membrane anchors in the nanodisc platform. Although the majority of the N-terminal transmembrane helix is present in our construct but not detected by MS, it is possible that a full length CYP3A4 with the additional 10 residues at the N-terminus could interact even more strongly with the membrane and increase the strength of the localized interactions with the A-helix and $\beta 1,2$ and F′G′-regions. This in turn could conceivably pull the F- and G-helix into slightly more intimate contact with the membrane. However, it is unlikely that the F- and G-helices, which are remote from the point of N-terminal insertion into the membrane, would have dramatically altered dynamics.

Functional Epitopes and Channels in CYP3A4

The H/ DX data are best considered in the context of functional regions or "epitopes" that contribute to ligand access or other behaviors. Some of these functional epitopes are

summarized in Figure 6. For example, Fishelovitch et al.[13,14] proposed an "aqueduct" for water access that is distinct from some substrate binding channels, in which Arg375 switches between conformations that provide a gating mechanism for access of water to the heme. Others have observed this possible gating mechanism in MD simulations in the membrane as well.[17] The channel, including Arg375, is lined by G436, S437, G438, P439, R440, N441, and C442 of the heme binding domain located in a loop connecting helices L and K′; Y99, T103, R105, and N104 of the BC loop near the C-terminal end of the B helix; and W126 and K127 of the C helix. The putative aqueduct is shown in Figure 6A with side chain atoms of these residues shown as spheres to aid in visualizing the site. The side chains and main chain atoms are color coded according to the relative solvent accessibility of the relevant amides at 10 min. Interestingly, the aqueduct is not "hyperaccessible" to solvent when CYP3A4 is in nanodiscs. In particular, one side of the proposed aqueduct exhibits minimal H/DX, but the other side exhibits moderately high exchange, as indicated by the yellow and orange atoms respectively (35%–40% exchange). The channel appears sufficiently solvent accessible to provide access of water to the heme, but it is not, for example, as solvent accessible as the F/G-helices, which exchange as much as 60% of their amide deuterons in the same time frame.

Our solvent accessibility data are also consistent with other solvent channels suggested on the basis of simulations. Fishelovitch and colleagues[13] suggest a number of substrate access channels, and they identify specific residues in each of the channels. We have found that the peptides bordering each of these channels, in particular the major channel forming residues that comprise channels "3" and "S", correlate well with peptides that have relatively high solvent accessibility, supporting the potential ease of access into the active site by these routes, as highlighted in Figure 6B and C, respectively. On the basis of our data and the previous simulation studies, it appears that substrate access channels favoring the CYP3A4 face with the F/G-helices represent the major solvent access pathways into the active site.

Another structural element that has been implicated with potential importance in substrate access and turnover is the "Phe-cluster",[8] comprising F213, F215, F219, F220, F241, and F304. This cluster has been considered to contribute to a binding site near the active site but distinct from it. These residues are highlighted in Figure 6D with the color scheme that reflects the H/DX at 10 min. These residues fall into a medium to high exchange regime behind the F′/G′-helices, suggesting that these too may have a moderate degree of solvent accessibility and thus could provide an intermediate site of access of hydrophobic ligands to the active site.

Effects of Ligand on Functional Epitopes

The comparison of solvent exchange for these "epitopes" in the presence and absence of ketoconazole further reveals functionally relevant changes in solvent access to CYP3A4. Crystallographic studies have established that ligand binding to CYPs, including CYP3A4, can induce conformation changes throughout the protein.[8,9] Specifically, those studies highlighted the F/ G and F′/G′ helices as well as the C-terminal loop as regions with the greatest degree of conformational change. The comparison of the data acquired in the presence and absence of ketoconazole is summarized on the structure of CYP3A4 in Figure

5. A trend observed in this data set is that solvent accessibility changes are not localized to the active site, although there is a noticeable protective effect by ketoconazole binding in the I-helix, which becomes significantly less solvent accessible. In particular, the middle of the I-helix near the conserved O_2 binding site becomes less solvent accessible. A number of different parts of the protein are affected moderately by ketoconazole binding, which supports the likelihood of long-range ligand-induced effects throughout CYP3A4 upon binding. In addition to the I-helix, regions of CYP3A4 that become less solvent accessible include the G-helix and the loop connecting it to the F′/G′ region, as suggested by the crystallographic models. A region of interest with regard to ketoconazole binding is the aqueduct channel discussed above. Solvent accessibility in the region containing residues in the aqueduct does not change (–2% < exchange <2%) upon ketoconazole binding with the exception of residues in the C-helix (126–127), which become more solvent accessible in the presence of ketoconazole. R375 (on the Beta1 sheet) is near a solvent accessible region, however.

The effect of ketoconazole on the H/DX of CYP3A4 is particularly noteworthy when considered in combination with the DSC, which indicates a very large increase in calorimetric enthalpy for denaturation upon addition of KTZ (Table 1). In the absence of large scale conformational changes, such an increase H is consistent with an increased stabilizing interactions with the membrane that would also decrease H/ DX, as suggested for the G-helix and the loop connecting the F′- and G′-helices. It is reasonable to speculate that these regions interact more tightly with the membrane upon KTZ binding. The proposed effects of ligand on membrane insertion of the local region around the F-G-loop are paralleled by studies that demonstrate the importance of amino acid sequence in this region in dictating membrane interactions of CYP2J2. MD simulations and mutagenesis with CYP2J2 suggest that the F-G-loop region is a critical determinant of the depth of insertion of the F-G region in a POPC lipid bilayer, further supporting our conclusions and the potential generality of membrane interactions across several CYP isoforms.[38]

A subtle but notable and interesting effect of KTZ binding is that there is no universal protective effect throughout. A few peptides exhibit increased solvent accessibility upon binding to ketoconazole, as shown in red in Figure 5. A region that becomes more solvent exposed upon binding is the C-helix, which is particularly interesting because this region contains one of the residues involved in cross-linking of CYP3A4 to Cyt b_5, which plays important supporting roles in the metabolism of many CYP3A4 substrates, as highlighted in Figure 6E.[39,40] This region's involvement in both conformational change upon ligand binding (Figure 5) and direct linkage to Cyt b_5 suggests the interesting possibility that Cyt b_5 binding and substrate binding could be energetically coupled.

It is interesting to compare our results with recent SAXS data for CYP3A4 in nanodiscs and with the few other H/DX experiments on CYPs in solution. The recently published low resolution structure of CYP3A4 in a nanodisc based on SAXS is potentially informative regarding our results.[41] The ensemble of SAXS structures suggests that the globular domain of CYP3A4 interacts minimally with the lipid surface of the nanodiscs and that it does not interact significantly with the scaffold protein. Notably, the structures based on SAXS suggest that the *G*′-helix interacts with the membrane surface near the rim of the nanodisc,

consistent with our H/DX data that indicate that the G′-helix is among the least dynamic or the least solvent exposed elements. The monotopic interaction of CYP3A4 with the membrane surface suggested by SAXS is consistent with the H/ DXMS data. Regarding H/ DXMS, an elegant study with CYP101 (P450cam) demonstrates redox-dependent H/DX in some structural elements.[42] The ferrous enzyme exhibited a reduction in dynamics and appears more rigid, to the extent that H/DXMS reports on dynamics. For the ferric enzyme, our results agree with those from P450cam suggesting that the soluble and membrane-bound CYPs are not very different with regard to solvent access channels. Because of the additional technical challenges of H/DX in the presence of nanodiscs, we have not yet performed experiments with the reduced CYP3A4. However, with the methods established to perform H/DXMS of CYP3A4 in nanodiscs, many redox states and ligand states may now be interrogated. The other isoforms studied by H/DX were CYP2B4 and CYP2B6, but those studies were done only in the absence of a membrane.[43] In those studies, several ligands caused larger changes in H/DX than we observe with CYP3A4, for some peptides including the F- and G- regions and the B/C loop. In summary, these results provide the experimental basis to assess peptide-specific dynamics and solvent accessibility for CYP3A4 in a native-like membrane environment. It is particularly striking that the F- and G-helices are among the most solvent accessible regions in both environments, as suggested by some MD simulations in model membranes, in a manner inconsistent with their being deeply embedded in the membrane. Overall, the model presented in Figure 2 based on multiple MD simulations[17,34] is consistent with all of the H/DXMS data. The elements most intimately embedded in the membrane appear to be the G′-helix, portions of the F′-helix, and A-anchor.

In light of the high hydrophobicity of the F- and G-helices, it is reasonable to speculate that hydrophobic ligands that enter the CYP3A4 active site from the membrane rely on transient interactions between these regions and the membrane. The DSC suggests these interactions are modulated by the ligand, particularly in the G-helix. The comparison of HDX in detergent vs in the nanodiscs membranes indicates that the membrane may uniquely control dynamics of the F- and G-helix regions, which are different in the detergent solubilized state.

Supplementary Material

Refer to Web version on PubMed Central for supplementary material.

Acknowledgments

ABBREVIATIONS

CYP3A4	cytochrome P4503A4
DSC	differential scanning calorimetry

HDXMS	H/D exchange mass spectrometry
MSP	membrane scaffold protein
POPC	1-palmitoyl-2-oleoyl-*sn*-glycero-3-phosphocholine

References

1. Wienkers LC, Heath TG. Predicting in vivo drug interactions from in vitro drug discovery data. Nat Rev Drug Discovery. 2005; 4:825–833. [PubMed: 16224454]

2. Ortiz de Montellano, PR. Cytochrome P450: Structure, Mechanism, and Biochemistry. 3. Plenum Publishing; New York: 2004.

3. Guengerich FP. Cytochrome P-450 3A4: Regulation and role in drug metabolism. Annu Rev Pharmacol Toxicol. 1999; 39:1–17. [PubMed: 10331074]

4. Wang RW, Newton DJ, Liu N, Atkins WM, Lu AY. Human cytochrome P-450 3A4: in vitro drug-drug interaction patterns are substrate-dependent. Drug Metab Dispos. 2000; 28:360–366. [PubMed: 10681383]

5. Johnson EF, Stout CD. Structural diversity of eukaryotic membrane cytochrome p450s. J Biol Chem. 2013; 288:17082–17090. [PubMed: 23632020]

6. Luthra A, Denisov IG, Sligar SG. Spectroscopic features of cytochrome P450 reaction intermediates. Arch Biochem Biophys. 2011; 507:26–35. [PubMed: 21167809]

7. Frank DJ, Denisov IG, Sligar SG. Analysis of Heterotropic Cooperativity in Cytochrome P450 3A4 Using a-Naphthoflavone and Testosterone. J Biol Chem. 2011; 286:5540–5545. [PubMed: 21177853]

8. Williams PA, Cosme J, Vinkovic DM, Ward A, Angove H, Day PJ, Vonrhein C, Tickle IJ, Jhoti H. Crystal Structures of Human Cytochrome P450 3A4 Bound to Metyrapone and Progesterone. Science. 2004; 305:683–686. [PubMed: 15256616]

9. Ekroos M, Sjögren T. Structal basis for ligand promiscuity in cytochrome P450 3A4. Proc Natl Acad Sci U S A. 2006; 103:13682–13687. [PubMed: 16954191]

10. Denisov IG, Shih AY, Sligar SG. Structural Differences Between Soluble and Membrane Bound Cytochrome P450s. J Inorg Biochem. 2012; 108:150–158. [PubMed: 22244217]

11. Cojocaru V, Winn PJ, Wade RC. The Ins and Outs of Cytochrome P450s. Biochim Biophys Acta, Gen Subj. 2007; 1770:390–401.

12. Wade RC, Winn PJ, Schlichting I, Sudarko. A Survey of Active Site Access Channels in Cytochromes P450. J Inorg Biochem. 2004; 98:1175–1182. [PubMed: 15219983]

13. Fishelovitch D, Shaik S, Wolfson HJ, Nussinov R. Theoretical Characterization of Substrate Access/Exit Channels in the Human Cytochrome P450 3A4 Enzyme: Involvement of Phenylalanine Residues in the Gating Mechanism. J Phys Chem B. 2009; 113:13018–13025. [PubMed: 19728720]

14. Fishelovitch D, Shaik S, Wolfson HJ, Nussinov R. How does the Reductase Help to Regulate the Catalytic Cycle of Cytochrome P450 3A4 Using the Conserved Water Channel? J Phys Chem B. 2010; 114:5964–5970. [PubMed: 20387782]

15. Isin EM, Guengerich EM. Substrate Binding to Cytochromes P450. Anal Bioanal Chem. 2008; 392:1019–1030. [PubMed: 18622598]

16. Conner KP, Woods CM, Atkins WM. Interactions of Cytochrome P450s with their Ligands. Arch Biochem Biophys. 2011; 507:56–65. [PubMed: 20939998]

17. Baylon JL, Lenov IL, Sligar SG, Tajkhorshid E. Characterizing the Membrane-Bound State of Cytochrome P450 3A4- Structure, Depth of Insertion, and Orientation. J Am Chem Soc. 2013; 135:8542–8551. [PubMed: 23697766]

18. Woods CM, Fernandez C, Kunze KL, Atkins WM. Allosteric Activation of cytochrome P450 3A4 by a-naphthoflavone: branch point regulation revealed by isotope dilution analysis. Biochemistry. 2011; 50:10041–10051. [PubMed: 22004098]

19. Gillam EM, Baba T, Kim BR, Ohmori S, Guengerich FP. Expression of modified human cytochrome P450 3A4 in Escherichia coli and purification and reconstitution of the enzyme. Arch Biochem Biophys. 1993; 305:123–131. [PubMed: 8342945]

20. Omura T, Sato R. A new cytochrome in liver microsomes. J Biol Chem. 1962; 23:1375–1376. [PubMed: 14482007]

21. Bass BJ, Denisov IG, Sligar SG. Homotropic cooperativity of monomeric cytochrome P450 3A4 in a nanoscale native bilayer environment. Arch Biochem Biophys. 2004; 430:218–228. [PubMed: 15369821]

22. Ritchie TK, Grinkova YV, Bayburt TH, Denisov IG, Zolnerciks JK, Atkins WM, Sligar SG. Reconstitution of membrane proteins in phospholipid bilayer nanodiscs. Methods Enzymol. 2009; 464:211–231. [PubMed: 19903557]

23. Nath A, Grinkova YV, Sligar SG, Atkins WM. Ligand Binding to Cytochrome P450 3A4 in Phospholipid Bilayer Nanodiscs: The Effect of Model Membranes. J Biol Chem. 2007; 282:28309–28320. [PubMed: 17573349]

24. Hebling CM, Morgan CR, Stafford DW, Jorgenson JW, Rand KD, Engen JR. Conformational Analysis of Membrane Proteins in Phospholipid Bilayer Nanodiscs by Hydrogen Exchange Mass Spectrometry. Anal Chem. 2010; 82:5415–5419. [PubMed: 20518534]

25. Parker CH, Morgan CR, Rand KD, Engen JR, Jorgenson JW, Stafford DW. A Conformational Investigation of Propeptide Binding to the Integral Membrane Protein γ-Glutamyl Carboxylase Using Nanodisc Hydrogen Exchange Mass Spectrometry. Biochemistry. 2014; 53:1511–1520. [PubMed: 24512177]

26. Fields PA. Protein function at thermal extremes: balancing stability and flexibility. Comp Biochem Physiol, Part A: Mol Integr Physiol. 2001; 129:417–431.

27. Brandts JF, Lin LN. Study of strong to ultratight protein interactions using differential scanning calorimetry. Biochemistry. 1990; 29:6927–6940. [PubMed: 2204424]

28. Schuler MA, Denisov IG, Sligar SG. Nanodiscs as a new tool to examine lipid-protein interactions. Methods Mol Biol. 2013; 974:415–433. [PubMed: 23404286]

29. Bayburt TH, Grinkova YV, Sligar SG. Self-Assembly of Discoidal Phospholipid Bilayer Nanoparticles with Membrane Scaffold Proteins. Nano Lett. 2002; 2:853–856.

30. Wales TE, Engen JR. Hydrogen exchange mass spectrometry for the analysis of protein dynamics. Mass Spectrom Rev. 2006; 25:158–170. [PubMed: 16208684]

31. Denisov IG, McLean MA, Shaw AW, Grinkova YV, Sligar SG. Thermotropic phase transition in soluble nanoscale lipid bilayers. J Phys Chem B. 2005; 109:15580–15588. [PubMed: 16852976]

32. Shaw AW, McLean MA, Sligar SG. Phospholipid phase transitions in homogeneous nanometer scale bilayer discs. FEBS Lett. 2004; 556:260–264. [PubMed: 14706860]

33. Marty MT, Zhang H, Cui W, Gross ML, Sligar SG. Interpretation and deconvolution of nanodisc native mass spectra. J Am Soc Mass Spectrom. 2014; 25:269–277. [PubMed: 24353133]

34. Berka K, Paloncýová M, Anzenbacher P, Otyepka M. Behavior of Human Cytochrome P450 on Lipid Membranes. J Phys Chem B. 2013; 117:11556–11564. [PubMed: 23987570]

35. Bartucci R, Guzzi R, Esmann M, Marsh D. Water penetration profile at the protein-lipid interface in Na,K-ATPase membranes. Biophys J. 2014; 107:1375–1382. [PubMed: 25229145]

36. Kakuda Y, Mueller DD. Effects of net charge on the hydrogen-deuterium exchange parameters of lysozyme. Arch Biochem Biophys. 1975; 171(2):586–596. [PubMed: 965]

37. Zhao C, Gao Q, Roberts AG, Shaffer SA, Doneanu CE, Xue S, Goodlett DR, Nelson SD, Atkins WM. Cross-Linking Mass Spectrometry and Mutagenesis Confirm the Functional Importance of Surface Interactions between CYP3A4 and Holo/Apo Cytochrome b_5. Biochemistry. 2012; 51:9488–9500. [PubMed: 23150942]

38. McDougle DR, Baylon JL, Meling DD, Kambalyal A, Grinkova YV, Hammernik J, Tajkhorshid E, Das A. Incorporation of charged residues in the CYP2J2 F-G loop disrupts CYP2J2-lipid bilayer interactions. Biochim Biophys Acta, Biomembr. 2015; 1848(10 Pt A):2460–2470.

39. Clarke TA, Im SC, Bidwai A, Waskell L. The role of the length and sequence of the linker domain of cytochrome b5 in stimulating cytochrome P450 2B4 catalysis. J Biol Chem. 2004; 279:36809–36818. [PubMed: 15194706]

40. Dürr UH, Yamamoto K, Im SC, Waskell L, Ramamoorthy A. Solid-state NMR reveals structural and dynamical properties of a membrane-anchored electron-carrier protein, cytochrome b5. J Am Chem Soc. 2007; 129:6670–6671. [PubMed: 17488074]

41. Skar-Gislinge N, Kynde SA, Denisov IG, Ye X, Lenov I, Sligar SG, Arleth L. Small-angle scattering determination of the shape and localization of human cytochrome P450 embedded in a phospholipid nanodisc environment. Acta Crystallogr, Sect D: Biol Crystallogr. 2015; 71(Pt 12): 2412–2421. [PubMed: 26627649]

42. Hamuro Y, Molnar KS, Coales SJ, OuYang Bo, Simorellis AK, Pochapsky TC. Hydrogen-deuterium exchange mass spectrometry for investigation of backbone dynamics of oxidized and reduced cytochrome P450cam. J Inorg Biochem. 2008; 102:364–370. [PubMed: 18023482]

43. Wilderman PR, Shah MB, Liu T, Li S, Hsu S, Roberts AG, Goodlett DR, Zhang Q, Woods VL Jr, Stout CD, Halpert JR. Plasticity of Cytochrome P450 2B4 as Investigated by Hydrogen-Deuterium Exchange Mass Spectrometry and X-ray Crystallography. J Biol Chem. 2010; 285:38602–38611. [PubMed: 20880847]
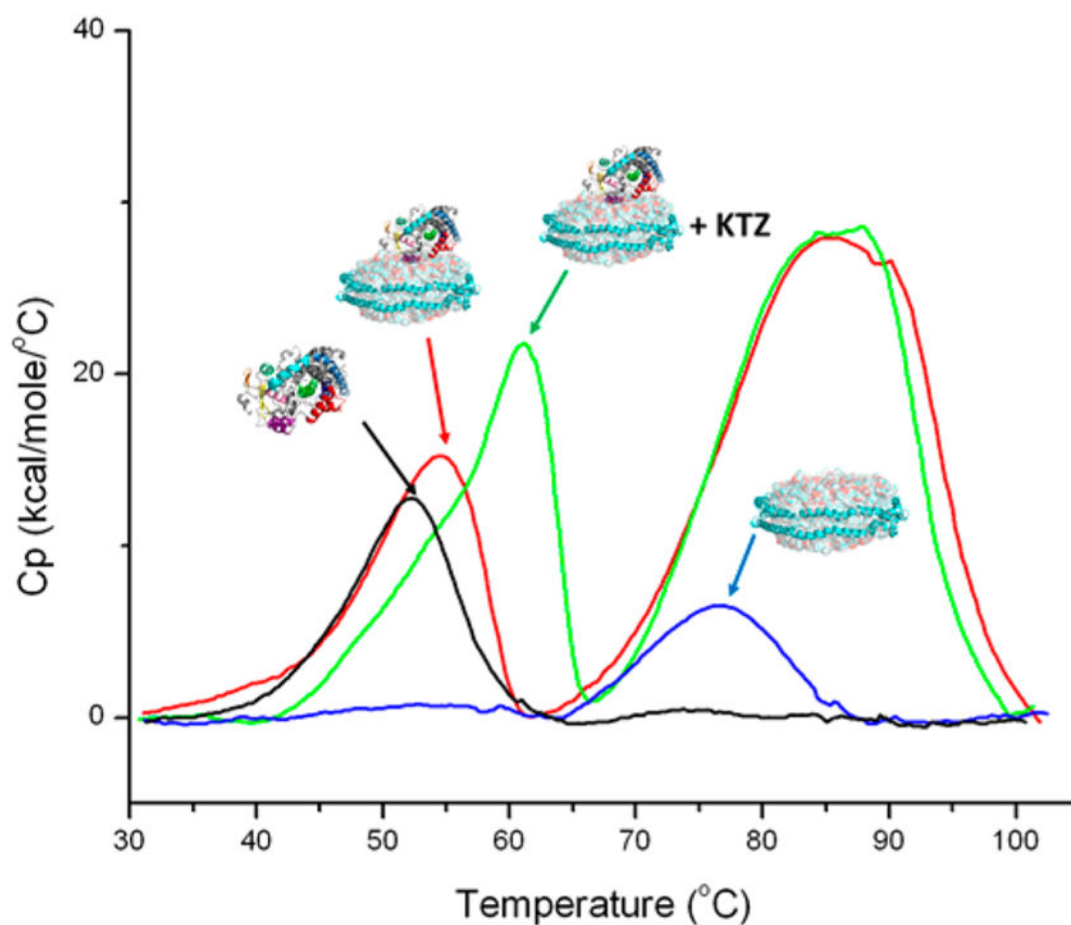
Figure 1.
Differential scanning calorimetry of CYP3A4 nanodiscs. Thermograms are shown for empty nanodiscs (blue), CYP3A4 in buffer without nanodiscs (black), CYP3A4 nanodiscs in the absence of ligand (red), and CYP3A4 nanodiscs with ketoconazole (green). All samples were 5 μM with respect to CYP3A4, CYP3A4 nanodisc, or empty nanodisc. The thermal transitions above 65 °C are due to nanodisc denaturation, which is stabilized slightly by the presence of CYP3A4. Transitions between 45 °C–65 °C are due to CYP3A4, which is stabilized by ketoconazole. The thermally resolved denaturation of CYP3A4 and the nanodisc indicates that CYP3A4 is not deeply embedded in the nanodisc membrane. However, the shift to higher T_m of the nanodisc in the CYP3A4 nanodiscs (red curve vs blue curve) indicates that the CYP3A4 remains associated with, and stabilizes, the nanodisc after CYP3A4 has denatured. All nanodisc or CYP3A4 nanodisc concentrations were 5 μM. The calorimetric enthalpies for the resolved transitions are reported in Table 1.
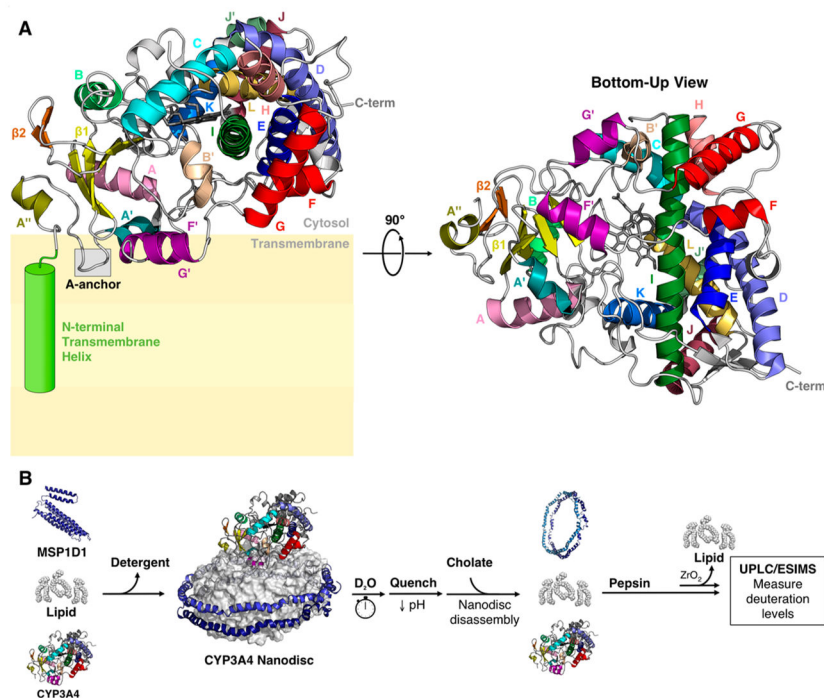
Figure 2.
CYP3A4 membrane model and HDX workflow. (A) Ribbon structure of CYP3A4 (PDB: 1TQN) oriented on a membrane interface (left). The membrane is depicted by the shaded yellow region. The green cylinder represents the membrane helix of residues 13–27, which are included in the protein used throughout this work, but are not recovered in the H/DX experiments. The second structure is rotated 90° to show the distal face (right). The perspective is from the membrane into the active site, and the membrane helix is omitted. The left orientation is similar to the orientation suggested in ref 17, which is supported by the data presented here. This orientation is used frequently throughout this article. Helices are individually labeled and colored: A″-helix, deep olive; A′-helix, deep teal; A-helix, pink; B-helix, lime green; B′-helix, tan; C-helix, cyan; D-helix, slate; E-helix, blue; F/G helices, red; F′/G′ helices, purple; H-helix, salmon; I-helix, forest green; J-helix, raspberry; J′-helix, pale green; K-helix, marine; L-helix, gold; β1-sheets, yellow; and β2-sheets, orange. The A-anchor is boxed in and labeled in the left view. The cytosolic and membrane-embedded components are labeled along the schematized membrane surface in black. The membrane anchor residues 1–2 and 13–27 of full length CYP3A4 are contained in the construct used for all experiments but are not shown. These residues extend from the point labeled "N-term" and are expected to penetrate into the membrane. (B) Workflow detailing protein-bound nanodisc formation and subsequent HDX labeling, quenching, disassembly, and peptic digest steps used to generate samples for mass spectrometry.
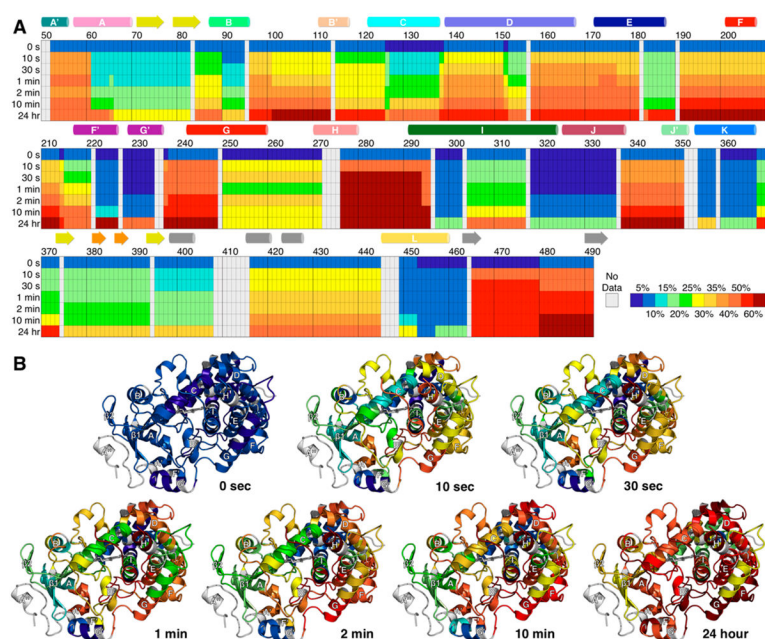
Figure 3.
Time-dependent HDX data for ligand-free CYP3A4 in nanodiscs. (A) Summarized residue-by-residue HDX exchange data for CYP3A4 at time points of 0 s, 10 s, 30 s, 1 min, 2 min, 10 min, and 24 h. The percent deuteration level was calculated by dividing the observed deuterium uptake by the theoretical maximum deuterium uptake for each peptide (number of residues – number of prolines – 1). Gray regions where no peptide was identified in these experiments and colors correspond to a range of percent deuteration as shown in the legend at the bottom. The secondary-structure elements are shown above their corresponding position in the sequence and are colored using the same scheme as that in Figure 2A. Residues 1–2, 13–50, and 493–503 are present in the protein studied but are not shown in the heat map because no H/D exchange data were recovered for them. (B) Solvent accessibility data mapped onto the crystal structure of CYP3A4 (PDB: 1TQN) for each time point. Colors used are the same as those indicated in A. The crystal structure begins at residue 28 and does not include the N-terminal transmembrane helix (27 residues; green cylinder in Figure 2). Residues 1–2 and 13–27 of the N-terminal transmembrane helix are present in the protein studied, but they were not recovered, and no H/D exchange data were recovered for them.
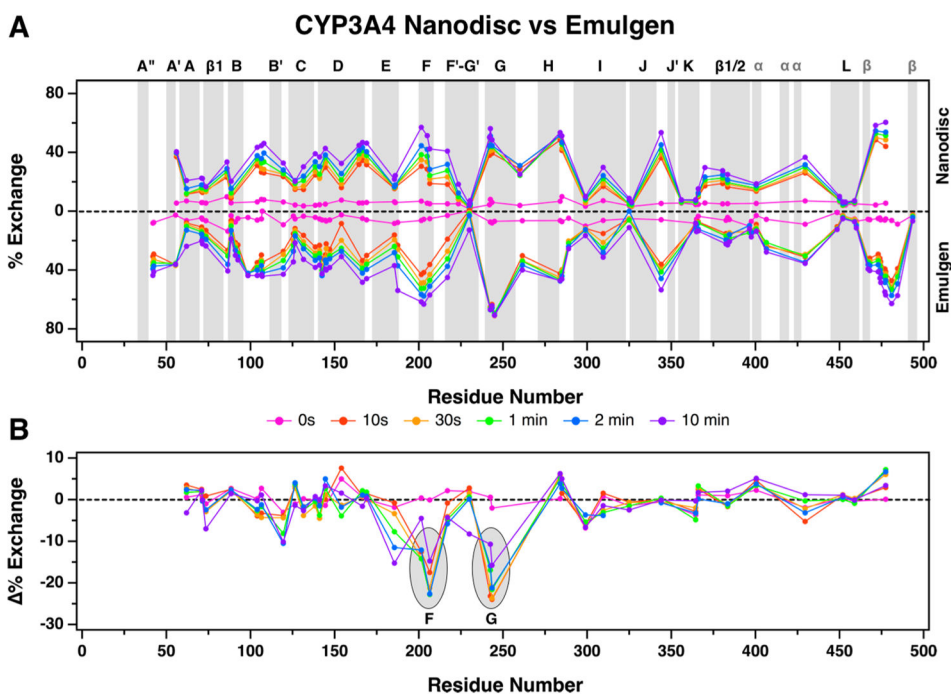
Figure 4.
HDX comparison of ligand-free CYP3A4 nanodiscs versus detergent solubilized CYP3A4. (A) The butterfly plot shows deuterium exchange profiles of ligand-free CYP3A4 nanodiscs (top) vs detergent solubilized CYP3A4 (bottom). Percent uptake for each time point is plotted at the midpoint of the primary sequence for each peptide. For example, uptake for the peptide spanning residues 33 to 51 is plotted at 42. The alpha-helices and beta-sheets are highlighted in gray and labeled above the plot. Generic "α" and "β" labels in gray are given to helices and sheets that are not named in this article, respectively. (B) A plot of the differences between matching peptides of CYP3A4 in nanodiscs and detergent solubilized CYP3A4 at each time point. The difference plot highlights regions of CYP3A4 nanodiscs that are more (positive value) or less (negative value) solvent accessible compared to detergent solubilized CYP3A4. Differences are not plotted when matching peptides do not exist between states. For example, no difference is calculated for the peptide spanning residues 33–51 because there was no peptide observed in that region for CYP3A4 nanodiscs.
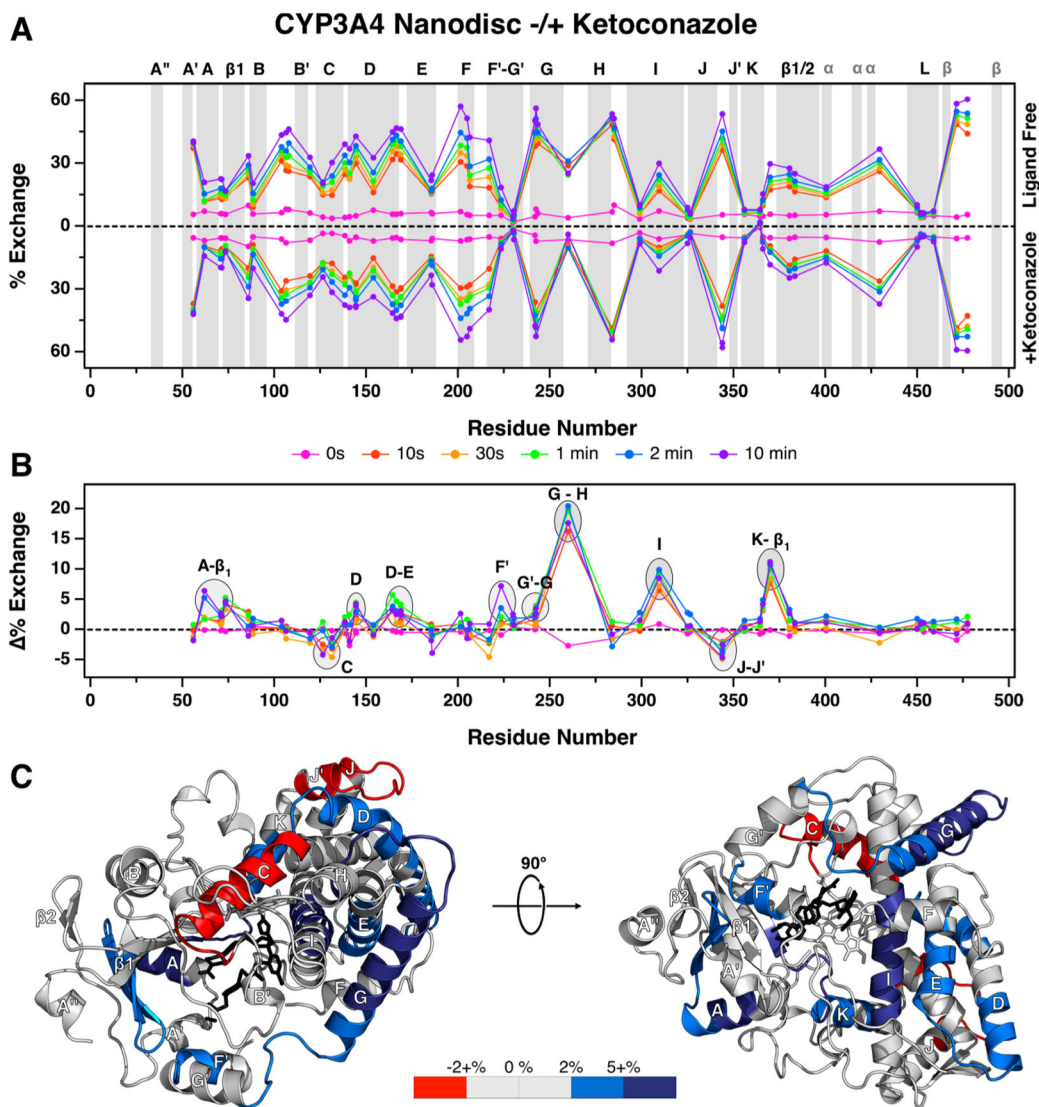
Figure 5.
HDX comparison of ligand-free CYP3A4 nanodiscs versus ketoconazole bound CYP3A4 nanodiscs. (A) The butterfly plot shows deuterium exchange profiles of ligand-free CYP3A4 nanodiscs (top) vs ketoconazole bound CYP3A4 nanodiscs (bottom). Percent uptake for each time point is plotted at the midpoint of the primary sequence for each peptide. (B) A plot of the differences between matching peptides of CYP3A4 in nanodiscs and detergent solubilized CYP3A4 at each time point. The difference plot highlights regions where solvent accessibility increases (negative value) or decreases (positive value) upon ketoconazole binding. (C) Solvent accessibility change data for CYP3A4-ketoconazole binding mapped onto the ketoconazole-bound crystal structure (PDB: 2V0M). Ketoconazole is shown in stick representation in black. Peptides in blue highlight modest decreases in solvent accessibility upon ketoconazole binding (2–5% above axis), peptides in dark blue highlight large decreases in solvent accessibility upon ketoconazole binding (>5% above axis), and peptides in red highlight modest increases in solvent accessibility upon ketoconazole binding (2–5%

below axis). The second structure is a 90° rotation of the first structure showing the distal face of CYP3A4.
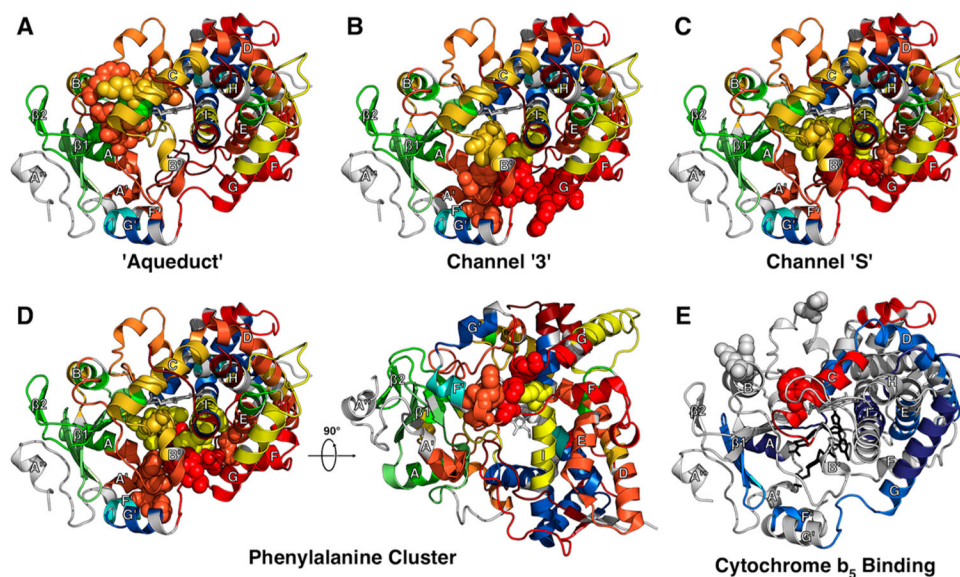
Figure 6.
Channels and sites of interest in CYP3A4. The relevant side chains for each structure are highlighted to help visualize their position in the structure. The membrane helix represented by the green cylinder in Figure 2 is present in the protein studied but is omitted here for clarity. (A) Water "aqueduct" residues, noted specifically by Fishelovitch and colleagues,[14] Y99, T103, N104, R105, W126, K127, R375, and G436 through C442, shown in spheres with the 10 min exchange data set for ligand-free CYP3A4. (B) Channel "3" residues, as described specifically by Fishelovitch and colleagues,[13] F108, S119, I120, K209, R212, F213, F215, F219, F220, V240, F241, P242, R243, V245, and F304, shown in spheres on the 10 min exchange data set for ligand-free CYP3A4. (C) Channel "S" residues, as described specifically by Fishelovitch and colleagues,[13] S119, K173, L211, R212, F213, E308, T309, S311, S312, I369, A370, M371, L482, L483, and Q484, shown in spheres on the 10 min exchange data set for ligand-free CYP3A4. (D) Phe-cluster residues F213, F215, F219, F220, F241, and F304 highlighted in spheres in the 10 min exchange data set. This is also shown with a 90° rotation to show the distal face. (E) CYP3A4 residues implicated in Cyt b$_5$ cross-linking,[37] K91, K96, K127, and K421 highlighted in spheres on the CYP3A4 structure depicting the effects of ketoconazole as shown in Figure 3.

Table 1

Model Independent Differential Scanning Calorimetry Parameters

system/species	T_m (C)		H_{cal} (cal/mol)[a]	
	CYP3A4	nanodisc	CYP3A4	nanodisc
CYP3A4 in buffer	52.6		8.9×10^4	
CYP3A4 in nanodiscs	56.7	85.8	1.8×10^5	5.5×10^5
CYP3A4 in buffer + KTZ[b]	54.4		9.0×10^4	
CYP3A4 in nanodiscs + KTZ	62.6	87.9	3.6×10^5	5.0×10^5
nanodisc		76.8		7.9×10^4

[a]Calorimetric enthalpy.

[b]50 μM ketoconazole.